

## THE FORMATION AND EVOLUTION OF INTRACLUSTER LIGHT

CRAIG S. RUDICK, J. CHRISTOPHER MIHOS, AND CAMERON MCBRIDE<sup>1</sup>

Department of Astronomy, Case Western Reserve University, 10900 Euclid Ave, Cleveland, OH 44106

*Draft version October 2, 2018*

### ABSTRACT

Using  $N$ -body simulations, we have modeled the production and evolution of diffuse, low surface brightness intracluster light (ICL) in three simulated galaxy clusters. Using an observational definition of ICL to be luminosity at a surface brightness  $\mu_V > 26.5$  mag/arcsec<sup>2</sup>, we have found that the fraction of cluster luminosity contained in ICL generally increases as clusters evolve, although there are large deviations from this trend over short timescales, including sustained periods of decreasing ICL luminosity. Most ICL luminosity increases come in short, discrete events which are highly correlated with group accretion events within the cluster. In evolved clusters we find that  $\approx 10$ –15% of the clusters' luminosity is at ICL surface brightness. The morphological structure of the ICL changes with time, evolving from a complex of filaments and small-scale, relatively high surface brightness features early in a cluster's history, to a more diffuse and amorphous cluster-scale ICL envelope at later times. Finally, we also see a correlation between the evolution of ICL at different surface brightnesses, including a time delay between the evolution of faint and extremely faint surface brightness features which is traced to the differing dynamical timescales in the group and cluster environment.

*Subject headings:* galaxies: clusters: general — galaxies: evolution — galaxies : interactions — galaxies: kinematics and dynamics — methods: N-body simulations

### 1. INTRODUCTION

Diffuse, intracluster starlight (ICL) consists of stars in galaxy clusters which have been gravitationally stripped from their parent galaxies via cluster galaxies interacting with other galaxies or with the cluster potential. As a product of the dynamical interactions within the cluster, the ICL has the potential to reveal a great deal of information about the cluster's accretion history and evolutionary state, as well as the mass distribution of cluster galaxies and the cluster as a whole. The quantity, morphology, and kinematics of the ICL each hold potentially useful information on the cluster's evolution, and processes affecting individual galaxies can be traced using individual ICL streams.

Observationally, ICL has been detected in numerous galaxy clusters in the local universe through broadband imaging. Early measurements of ICL (Zwicky 1951; Oemler 1973; Gudehus 1989) were extremely difficult due to the very low surface brightness of ICL features, at less than 1% of sky brightness. The advent of modern techniques for precision CCD photometry has caused a resurgence of interest in the subject (e.g., Uson et al. 1991; Gonzalez et al. 2000; Feldmeier et al. 2002, 2004; Da Rocha & de Oliveira 2005). Dozens of clusters from the very nearby universe, such as Virgo (Mihos et al. 2005) and Coma (Adami et al. 2005), to the intermediate redshift universe (Vílchez-Gómez et al. 1994; Zibetti et al. 2005) have now been studied for signs of intracluster luminosity. Most studies estimate that the ICL comprises  $\approx 10$ –40% of the clusters' luminosity, and it is now thought that ICL is a ubiquitous feature of evolved galaxy clusters.

The ICL can also be studied using discrete tracers of stellar populations, such as intracluster planetary nebulae (IPNe) (e.g. Arnaboldi et al. 1996, Feldmeier et al. 1998, Aguerri et al. 2005), red giants (Durrell et al. 2002), novae (Neill

et al 2005), and supernovae (Gal-Yam et al. 2003). These studies of individual intracluster stars are generally limited to the nearby universe due to the extreme difficulty in detecting these objects. However, estimates of ICL luminosity using these methods are in broad agreement with those found through broadband imaging. Of these stellar tracers, IPNe are especially interesting as radial velocity measurements of IPNe have opened up the possibility of studying the kinematics of the ICL (Arnaboldi et al. 2004; Gerhard et al. 2005).

While the existence of ICL is now well established, questions remain surrounding the details of when, where, and how the ICL is formed. A variety of scenarios have been put forward to explain the production of ICL: stripping during the initial collapse of the cluster (e.g., Merrit 1984); stripping of galaxies by an established cluster potential (Byrd & Valtonen 1990; Gnedin 2003); stripping within galaxy groups accreting onto the cluster (Mihos 2004); and stripping from high speed encounters between cluster galaxies (Moore et al. 1996). Indeed in the complex environment of a collapsing and accreting galaxy cluster, all these processes likely contribute to the overall production of ICL, indicating that full  $N$ -body simulations of the cluster evolution are needed to probe ICL formation.

Motivated by these considerations, several recent studies have focused on simulating ICL production in a  $\Lambda$ CDM universe, using either dark matter simulations with tracer particles (e.g., Napolitano et al. 2003) or full hydrodynamical galaxy formation models (e.g., Murante et al. 2004; Willman et al. 2004; Sommer-Larsen et al. 2005) and have each found that at  $z = 0$ , at least 10% of the clusters' stars were unbound to any one galaxy, in line with current observations. Napolitano et al. (2003), Sommer-Larsen et al. (2005), and Willman et al. (2004) each study the kinematic distribution of the unbound stars and find significant kinematic substructure. Willman et al. (2004) make detailed simulated observations of IPNe and show that they can be used to trace specific tidal features.

Each of these studies, however, focuses on ICL defined as

Electronic address: craig@fafnir.astr.cwru.edu, mihos@case.edu, ckm8@pitt.edu

<sup>1</sup> Now in the Department of Physics and Astronomy, University of Pittsburgh.

stars which are unbound to any cluster galaxy. In general, the specific binding energy of individual stars is not a readily observable feature of the ICL. While IPNe are already proving useful in determining the kinematic structure of the ICL in nearby clusters, most observational studies continue to rely on broadband imaging to quantify the properties of the ICL. To make the connection between observations and simulations more direct, we adopt here a more observational definition of ICL: luminosity below a given surface brightness threshold. Using this definition, we study the ICL properties of three simulated galaxy clusters in a  $\Lambda$ CDM universe. We describe the simulation and artificial imaging techniques in Section 2, and Section 3 explores the mechanisms driving the evolution of the ICL.

## 2. SIMULATIONS

To simulate the formation of intracluster light we use a technique similar to that described by Dubinski (1998), but updated to reflect a modern  $\Lambda$ CDM cosmology, a mix of both spiral and elliptical galaxy types, and a halo subdivision scheme to avoid overly massive galaxies in the simulation. Full details of the simulation techniques will be given elsewhere (Mihos et al. in preparation); we highlight the most important features here.

To create the initial conditions for the cluster simulations, we first run a  $N = 256^3$   $50 \times 50 \times 50$  Mpc  $\Lambda = 0.7$ ,  $\Omega_M = 0.3$ ,  $H_0 = 70$  cosmological dark matter simulation from  $z = 50$  to  $z = 0$ , at which point collapsed clusters with masses  $O(10^{14})M_\odot$  are chosen to re-simulate at higher resolution. For each cluster, we identify individual halos at  $z = 2$  which are destined to end up within the  $z = 0$  cluster, and insert higher resolution collisionless galaxy models into these halos. Given a halo mass, we first decide the number of galaxies to insert using a Monte Carlo technique based on the ‘‘halo occupancy distribution’’ (HOD) formalism (Berlind & Weinberg 2002), in which the number of galaxies inserted into a halo of mass  $M$  is given by

$$N_{gal} = \begin{cases} \text{int}((M/M_{MW})^\alpha) & \text{if } M/M_{MW} > 1 \\ 1 & \text{if } 0.1 < M/M_{MW} < 1 \\ 0 & \text{if } M/M_{MW} < 0.1 \end{cases}$$

where the Milky Way mass is taken to be  $M_{MW} = 6 \times 10^{11} M_\odot$  and the HOD index is given by  $\alpha = 0.7$ .

For each substituted halo, the original dark matter particles (referred to as ‘‘cosmological dark matter’’) are sorted by environmental density and the 70% most dense particles are excised from the simulation, to be replaced with high resolution galaxy models. The remaining cosmological dark matter particles are left intact and fill the volume around each substituted galaxy model as an extended dark matter halo (for a single galaxy within a halo) or common dark matter envelope (for multiple galaxies within a halo). When multiple galaxies are substituted, the individual masses are drawn from a power law mass function, subject to the constraint that the total mass of all galaxies must be equal to the mass being substituted. The final galaxy mass function is set by the convolution of the underlying halo mass function, the HOD function, and the power-law function for substituting multiple galaxies, and shows a Schechter-like high mass cutoff (from the rarity of high mass halos) and behaves like a power law (slope  $\sim -1$ ) at lower masses. For halos with multiple galaxies inserted, the galaxy positions and velocities within the halo are determined by statistically sampling the densest subpeaks of the original dark matter halo.

When substituting galaxies, two types of models are used: a disk model in which the stars follow a composite exponential disk plus Hernquist (1990) bulge (with bulge-to-disk ratio of 1:5), and an elliptical galaxy model where the stars have a pure Hernquist (1990) distribution. The disk galaxy model is built using the prescription of Hernquist (1993), while the elliptical galaxy is built in a similar fashion, by omitting the disk component and using a massive spheroid instead. Both models are embedded in isothermal dark halos (referred to as ‘‘galaxy dark matter’’); these halos possess a constant density central core inside one disk scale length (for the disk galaxy model) or Hernquist scale radii (for the elliptical galaxy model), and a maximum extent of 10 scale lengths or scale radii. In these models, the galaxy dark matter mass is six times the stellar mass; when coupled with the extended cosmological dark matter mass left in the original halo, this gives the galaxies a dark-to-stellar mass ratio of 10:1. The galaxy models have been built in dynamical equilibrium (see Hernquist 1993 for details), and have been evolved in isolation for thirty half-mass rotation periods to ensure stability. We also track the detailed evolution of individual, relatively isolated galaxies within the full cluster simulation and see no evidence of any instability which might be caused by the insertion process itself.

The choice of whether to insert a spiral or elliptical model into any given halo is based on the local galaxy density, following the morphology-density relationship of Dressler (1980). We first calculate the local galaxy number density around each galaxy, then assign a galaxy type based on this galaxy density, where the fraction of ellipticals rises from 10% in the lowest density quartile to 40% in the upper quartile. For disk galaxy models, the orientation of the disk plane is randomly chosen. Given a galaxy mass, galaxy sizes are then scaled by  $M^{0.5}$  and velocities are scaled by  $M^{0.25}$ . This scaling preserves surface density and keeps spiral galaxies on a Tully-Fisher-like relationship. Applied to elliptical galaxies, this scaling introduces a slight tilt to the Fundamental Plane, but this tilt is modest given the limited range of initial galaxy masses used.

We illustrate the initialization process with statistics from one of our clusters. In this cluster, a total of 121 high resolution galaxy models (91 spirals and 30 ellipticals) were inserted into 80 dark halos. The number of particles used in each galaxy model scales with total galaxy mass, so that all star particles have the same mass. In total, the simulation consists of approximately 10 million particles: 5.4 million star particles, 2.4 million galaxy dark halo particles, and 2.2 million cosmological dark halo particles. The Plummer-equivalent gravitational softening length of the particles is set at 300 pc for stars, 1.4 kpc for galaxy dark matter, 10 kpc for cosmological dark matter, and 50 kpc for cosmological dark matter well outside the cluster (at  $r > 8$  Mpc). Initialized at a redshift of  $z = 2$ , the cluster is then evolved to  $z = 0$  using the  $N$ -body code GADGET (Springel et al. 2001).

In order to test the effects of the chosen galaxy substitution redshift, we have re-initialized one of our cluster at  $z = 3$  and compared its evolution to that of the standard cluster with substitution at  $z = 2$ . Due to the hierarchical nature of the growth of structure in the universe, the cluster at higher redshift contains dark matter halos which tend to be smaller than those found at lower redshift. Thus, in the high redshift cluster, fewer galaxies are inserted because fewer dark matter halos meet our minimum substitution mass, and the galaxies which are inserted tend to be systematically smaller due to the lower

dark halo masses. With these caveats in mind, we find that our results are quite similar in both simulations. All further results presented in this paper refer to clusters in which galaxies were substituted at  $z = 2$ .

We have simulated three such clusters, referred to throughout this paper as clusters C1, C2, and C3. Each cluster is a separate, unique object taken from the same cosmological simulation, selected to be of approximately the same mass. Thus, there are no systematic differences between the clusters, only variations in the initial mass distribution resulting from the cosmic variance of mass distribution within the simulation. Parameters of the individual clusters can be found in Table 1, including  $R_{200}$  (the radius within which the density of the cluster is 200 times the critical density),  $M_{200}$  (the mass enclosed in  $R_{200}$ ), the number of galaxies initially inserted at  $z = 2$ , and the number of galaxies remaining at  $z = 0$ .

To be sure, our simulation scheme is a simple caricature of the very complex process of galaxy cluster evolution. The use of collisionless models neglects the effects of gas accretion, ram pressure stripping, and star formation, all of which could act to alter the relative spatial distribution of stars in the evolving cluster. However, by concentrating on gravitational dynamics alone, we avoid the significant uncertainties involved with modeling gas physics, star formation, and feedback, and isolate the role that gravitational stripping plays in the creation of intracluster light. Another issue is our galaxy substitution scheme. Our low mass substitution limit corresponds to 10% of the Milky Way mass, meaning that our simulations are essentially focusing on the evolution of fairly massive galaxies; the stripping and destruction of low mass dwarf galaxies are not captured in our simulations. This may result in a systematic underestimate of the ICL fraction in our simulations, since the effects of tidal stripping are enhanced for dwarf galaxies (e.g., Moore et al. 1998). For a Schechter luminosity function with faint end slope  $\alpha = -1$ , galaxies below 0.1 Milky Way masses contribute about 10% of the total luminosity, placing an upper limit on the amount of ICL that we could be missing due to our substitution limit. Also, by choosing a redshift of  $z = 2$  for substitution, we miss halos which may be just below the substitution mass limit at  $z = 2$  but later grow to exceed the substitution limit. Because we do not insert galaxies in these halos, we miss their contribution to the ICL; however, since their host halos remain intact, they still contribute to the stripping of other galaxies, so that the dynamics of the substituted galaxies remains accurately tracked. With these caveats in mind, we now proceed to study the properties of diffuse light in these cluster simulations.

### 2.1. Simulated Images

To create the simulated cluster images, we project onto two dimensions the particle distribution, creating an image of  $4k \times 4k$  pixels, with each pixel 800 pc on a side. For each cluster we imaged 80 snapshots equally spaced in  $\log(\text{expansion factor})$  from  $z = 2$  to  $z = 0$ . We have labeled all simulated images in units of time, such that  $t = 1.0$  is the current age of the universe.

All simulated images and analyses were carried out using a fixed viewing angle; the effect of varying viewing angle on the derived properties of the ICL is examined below. In order to create a realistic, continuous mass distribution from our discrete particle data, we Gaussian smooth the particles in an SPH-like way, where each particle has smoothing length  $\sigma$  which is proportional to the local three-dimensional particle density. The proportionality constant determining how

the width of the Gaussian is scaled with density was determined by visual inspection of the images, in order to balance the competing effects of smoothing the particles enough to remove their discreteness, while not over-smoothing which can destroy legitimate spatial structures. The maximum distance to which any particle was smoothed was limited to the shorter of  $4\sigma$  or 400 kpc, and the final results are not highly sensitive to the detailed choice of the smoothing parameter value, over a wide range of qualitatively reasonable values.

Converting the projected mass distribution into a luminosity distribution requires applying a mass-to-light ratio ( $M/L$ ) based on the evolutionary state of the stellar population. This, however, requires assumptions about the star formation rate, the IMF, stellar evolutionary tracks, etc., none of which we have modeled in our  $N$ -body simulations. Additionally, an evolving  $M/L$  would have the effect of obscuring many aspects of the dynamical evolution of the cluster, by conflating dynamical changes with stellar evolutionary effects. For simplicity, we have instead chosen to use a fixed stellar mass to light ratio of  $5M_{\odot}/L_{\odot}$  for all of our images, a characteristic value for the  $V$ -band luminosity of an evolved stellar population such as we expect to comprise the ICL of a galaxy cluster in the local universe. One of the ramifications of using this constant  $M/L$  is that we are not attempting to simulate observations of the clusters at distant redshifts, but we are simulating observations of the clusters at a given point in their dynamical evolution, as they would appear at  $z = 0$ . This makes our simulated observations more relevant to observations of the local universe where there are many galaxy clusters at a variety of dynamical ages.

As noted in §1, many different working definitions have been proposed for the ICL, including material which is unbound to any cluster galaxy, material at very low surface brightness, and diffuse material which is morphologically distinct from extended envelopes around galaxies. Here we use a definition which is both quantifiable and observationally tractable: luminosity which has a  $V$ -band surface brightness fainter than  $26.5 \text{ mag/arcsec}^2$ . This limit coincides with the Holmberg radius (Holmberg 1958), a commonly used surface brightness limit defining the isophotal size of galaxies. This choice is further motivated by inspection of both our simulated images and of deep imaging of galaxy clusters (Mihos et al. 2005; Feldmeier et al. 2002), where  $\mu_V = 26.5$  is approximately the surface brightness limit where the isophotal contours no longer simply outline those at higher galaxian surface brightness. That is, this limit appears to be the surface brightness where the diffuse light takes on its own morphology, as opposed to being a continuation of the galaxies' extended profiles. In section §3.3 we also examine the evolution of ICL under a fainter choice of ICL threshold:  $\mu_V = 30$ .

Figure 1 shows an example of one of our simulated images, color coded by  $V$ -band surface brightness. Black represents all luminosity at  $\mu_V < 26.0 \text{ mag/arcsec}^2$ . Each other color represents a bin of one  $\text{mag/arcsec}^2$ : red is  $\mu_V = 26.0 - 27.0$ , orange is  $\mu_V = 27.0 - 28.0$ , etc. Our images do not show luminosity which is fainter than  $\mu_V = 33.0 \text{ mag/arcsec}^2$ . This same color scheme will be used in all simulated images shown in this paper. Also, at the top right of Figure 1, the distance scale of the image in physical units is shown.

Because our working definition of ICL is based on surface brightness, a projected property of the cluster, it is possible that our results could be sensitive to the choice of viewing angle. To test this effect, we measured the distribution of luminosity as a function of surface brightness for 7 different

viewing angles of each cluster at 3 different times. The 7 viewing angles used were our standard viewing angle used for analysis, plus rotations of  $\pi/4$ ,  $\pi/2$ , and  $3\pi/4$  in both the  $\theta$  and  $\phi$  directions. Figure 2 shows the fraction of the luminosity in each cluster which is in surface brightness bins of 1 mag/arcsec<sup>2</sup> at  $z = 1.0$  ( $t = 0.45$ ),  $z = 0.5$  ( $t = 0.64$ ), and  $z = 0.0$  ( $t = 1.0$ ). The points are the mean values and the error bars indicate the minimum and maximum values found in those 7 viewing angles. Over the timescales shown, the min-max error bars tend to be smaller than the separation between the means. This indicates that the physics of cluster evolution dominates over projection effects in the observed evolution of the clusters. The only case where the cluster evolution does not dominate projection effects is the evolution of C1 from  $z = 0.5$  to  $z = 0$ . We will see in §3.2, however, that this is the result of the specific evolution of this cluster.

Figure 2 also shows that as the cluster evolves, the fraction of luminosity at high surface brightness decreases while the fraction of luminosity at low surface brightness increases. This indicates that luminosity is being transferred from high to low surface brightness. The fraction of cluster luminosity at ICL surface brightness clearly increases with time. The mechanism driving this redistribution of luminosity is the stripping of material from galaxies to form the ICL. We will explore the production of ICL luminosity in more detail in §3

### 3. EVOLUTION AND PRODUCTION OF ICL

A full understanding of the nature of ICL requires measuring its evolution and exploring the mechanisms which drive this evolution. To this end, we have measured the luminosity of the ICL throughout the evolution of each of our clusters. Furthermore, we have searched for correlations between the changes in ICL luminosity and specific events in the clusters' evolution.

During the formation and evolution of galaxy clusters, a variety of gravitational processes act to liberate stars from galaxies, leading to the formation of the intracluster light. Slow interactions between galaxies in infalling groups (Mihos 2004), repeated fast interactions between galaxies inside the cluster (Moore et al 1996), tidal stripping of galaxies by the cluster potential (Byrd & Valtonen 1990), and interactions between galaxies and more massive substructures within the cluster (Gnedin 2003) all operate in concert to remove stars from their cluster galaxies. In cosmologically-generated simulations such as those presented here, where all these processes are at work, it is difficult to uniquely disentangle any one of these effects from the overall evolution of the system, and we make no attempt to do so here. Instead, since all these processes act to strip material from galaxies, we will generically refer to these combined processes as "gravitational stripping" and focus more on their net (observational) result rather than on the differing details of the gravitational dynamics involved in each one.

#### 3.1. Evolution of ICL Luminosity

The top portion of Figure 3 shows the fraction of the total luminosity in the cluster which is at  $\mu_V > 26.5$  ( $f_{ICL}$ ) as a function of time for all three clusters. The obvious trend is that the luminosity of the ICL increases with time in all the clusters, as material is stripped from galaxies as they first interact in the group environment, then later aggregate to form the cluster. On shorter timescales, however, there are significant deviations from the overall trend of increasing ICL luminosity fraction. The middle section of Figure 3 shows the fractional

change in ICL luminosity per unit time ( $\Delta f_{ICL}$  function), calculated by:

$$\Delta f_{ICL,i} = \left( \frac{f_{ICL,i} - f_{ICL,i-1}}{f_{ICL,i-1}} \right) (t_i - t_{i-1})^{-1} \quad (1)$$

There is a significant dispersion on short timescales in the  $\Delta f_{ICL}$  function. Each cluster experiences several significant events of *decreasing* ICL luminosity, with the major increases coming in short, large events. In §3.2 we will show that these large increases correlate very strongly with major accretion or collisional events between galaxies and galaxy groups within the cluster, while the decreases are caused by material initially collapsing into higher density environments, thus temporarily raising its surface brightness.

The bottom plot in Figure 3 shows the running mean ( $\hat{\mu}$ ) and standard deviation ( $\hat{\sigma}$ ) of the  $\Delta f_{ICL}$  function, using a running bin of ten time points. The time plotted is the average of the time points in each bin. In each cluster, there is at least one point after  $t = 0.6$  where  $\hat{\mu}$  is negative. For even one point of the running mean to be negative, the clusters must be losing ICL luminosity on average over a significant period of their evolution (the size of one running bin). The width of the running bin in time units changes due to the logarithmic spacing of the data points, however after  $t = 0.6$  the minimum size of one bin is 0.075, or at least 11% of the cluster's evolution. This variability in the cluster's ICL luminosity evidences the complexity of the processes which produce the intracluster light.

#### 3.1.1. Initial Evolution of Cluster ICL

One clear feature in Figure 3 is the extremely similar behavior demonstrated by all three clusters at very early times ( $t < 0.35$ ). Each cluster displays a sharp decrease in ICL luminosity almost immediately at the start of the simulation, followed by a significant increase over a very short timescale. Because the galaxy models have been constructed in equilibrium, this behavior is not due to instabilities with the galaxies themselves.

We have verified this fact by visually examining isolated galaxies at the beginning of the simulation, and find very little evolution in them until they begin interacting with nearby neighbors. Instead, visual inspection shows that much of the early evolution in the cluster ICL is due to prompt interactions between small groups of galaxies. These groups are not necessarily in virial equilibrium, and several of them quickly collapse once the simulation is started by first compressing the galaxies, then tidally stripping material out to low surface brightness. Additionally, we have constructed the  $\Delta f_{ICL}$  function for these isolated systems and find that the structure of the  $\Delta f_{ICL}$  function for the entire cluster closely matches that of the the collapsing group environment. Thus, we find that the early evolution of the  $\Delta f_{ICL}$  function of the clusters is the result of the physics resulting from the initial collapse of galaxies in the group environment.

However, one should remain cautious about over-interpreting the clusters' behavior in the initial stages of our simulations. The initial luminosity distribution of the clusters is not entirely realistic, due to the somewhat artificial way in which we inserted isolated, unevolved galaxies into the cluster potential. Thus, we shall focus our analysis on the evolution of the clusters after  $t \approx 0.4$ , when the physics of cluster evolution should dominate over effects due to the initialization of the cluster and the prescription for inserting galaxies into the model.

### 3.2. Individual Clusters

While all of our model clusters demonstrate similar global trends, each has a unique dynamical history which manifests itself in the cluster’s luminosity evolution. By following the evolution of each cluster individually, we can identify the events which significantly impact the production of ICL.

#### 3.2.1. Cluster C1

The ICL evolution of C1 is characterized by large gains in ICL luminosity early in its history, between  $t = 0.4 - 0.6$ , followed by an extended period of very little activity. The early gains experienced by C1 are very similar to those of the other clusters. The  $\Delta f_{ICL}$  function is quite erratic in this region, showing both large gains and large losses occurring over short periods of time. This is further demonstrated by the  $\hat{\sigma}$  of the  $\Delta f_{ICL}$  function in this range, which is quite large.

Figure 4 shows a series of simulated images illustrating the evolution of C1, with a color scale identical to that used in Figure 1. In the early stages of cluster collapse, the many different galaxies are interacting in small groups, which later merge together to form the large cluster. With the complexity of these small-scale interactions taking place throughout the volume, it is extremely difficult to determine the impact individual events have on the evolution of ICL. Similarly complex behavior in the early stages of the simulations is seen in all of the clusters, as galaxies first collapse into groups; this generic result illustrates the importance of interaction in the group environment that begin the formation of the diffuse ICL well before the cluster as a whole has collapsed and virialized.

After  $t = 0.6$ , C1’s  $f_{ICL}$  is quite flat, and the  $\hat{\sigma}$  of the  $\Delta f_{ICL}$  function is much smaller than it is before this time. Only a few percent at most of the cluster luminosity is converted to ICL from  $t = 0.6 - 1$ . This extremely small increase in ICL luminosity is the result of the specific evolutionary history of the cluster, seen in Figure 4. By  $t = 0.6$ , three massive galaxy complexes have clearly developed. While it is difficult to determine from Figure 4 the internal structure of these complexes, in general they are groups dominated by a massive spheroidal galaxy, with several smaller galaxies in close proximity. The most striking aspect of the evolution of C1 at these later times is that these three massive complexes which formed by  $t = 0.6$  still exist intact and relatively unaltered at  $t = 1$ . In essence, there are no major accretion or interaction events taking place between the groups, and without these violent events to quickly add ICL, the ICL fraction rises only slowly at late times in this cluster.

#### 3.2.2. Cluster C2

The early luminosity evolution of C2 is quite similar to that of C1, as galaxies interact on group scales throughout the volume. However, whereas C1’s  $f_{ICL}$  flattens after  $t = 0.6$ , that of C2 continues to increase substantially with time. The  $\Delta f_{ICL}$  function of C2 is quite active throughout its evolution, with its  $\hat{\sigma}$  relatively large at all times.

Figure 5 shows simulated images of the evolution of C2. Whereas C1 quickly develops three distinct massive complexes, C2’s mass buildup consists many small groups continually coalescing to form one very large central mass complex. At  $t = 0.6$ , when the three mass complexes of C1 were in place, the major mass concentration in the upper right of C2 consists of many separate galaxies which are still in the process of merging. Additionally, there are three distinct galaxy groups to the lower left of the main mass which have yet to

be incorporated into the cluster core. As time progresses, the main mass concentration continues to consolidate through mergers, while the other outlying galaxies are each drawn into the concentration in turn. The large number of accretion events where massive galaxies and groups fall into the cluster center create the frequent, large increases in  $f_{ICL}$  which occur throughout C2’s evolution.

#### 3.2.3. Cluster C3

The evolution of C3 (Figure 6) provides the most dramatic example that the production of ICL luminosity is driven by merger events between massive groups of galaxies. As was the case in C1 and C2, the  $f_{ICL}$  of C3 is sporadic, but increasing overall, before  $t = 0.6$ . However, its subsequent evolution is quite unique. At  $t = 0.6$  there are 4 distinct massive groups which collapse into a single, very concentrated massive complex at  $t = 0.7$ . The rapidly changing tidal field of the collapsing cluster, coupled with many small-scale tidal interactions, leads to significant stripping of the cluster galaxies and an enormous rise in the  $f_{ICL}$  of C3 between  $t = 0.68$  and  $t = 0.8$ , where the ICL luminosity more than doubles.

It is also interesting to note the significant *decrease* in  $f_{ICL}$  as this strong “crash” of galaxies begins, starting at about  $t = 0.6$ . The decrease is due to the fact that as the galaxy groups collapse, the luminosity becomes highly concentrated. This concentration of luminosity elevates the surface brightness of much of the luminosity in the cluster; material below our  $\mu_V > 26.5$  definition for ICL is, for a short-time, boosted to brighter, non-ICL levels. While projection effects play some role in this phenomenon, it is also attributable to a real (but transient) rise in the physical density of luminous mass. A similar process is responsible for many of the major ICL luminosity decreases which are observed to precede major accretion events in the evolution of each of the clusters.

#### 3.2.4. Increased Time Resolution of an Accretion Event

To further illustrate that the evolution of the  $f_{ICL}$  is the result of interactions between massive galaxies and groups, Figure 7 shows one such event from C2 at higher time resolution. Figure 8 shows the corresponding regions of the  $f_{ICL}$  and  $\Delta f_{ICL}$  plots.

The major event that Figure 7 depicts is the accretion of a small galaxy group (indicated by the arrow) which is below and to the left of the main body of the cluster at  $t = 0.86$ . The series of images clearly shows this group moving through, interacting with, and exiting from the cluster core, resulting in a large net increase in ICL luminosity. Again, however, from  $t = 0.88$  to  $t = 0.9$ , the cluster actually loses ICL luminosity as the group moves closer to the cluster center. The situation is similar to that described in Section 3.2.3, whereby the increased surface brightness of the diffuse starlight is caused by both a temporary increase in the local density, as well as the projection of larger amounts of material onto the line of sight. As the group begins to exit the cluster center, at  $t = 0.92$  and  $0.93$ , the ICL luminosity increases slightly, driven largely by the fact that diffuse light in the cluster and group is no longer boosted in luminosity simply by projection. Immediately thereafter, however, we see larger gains in ICL luminosity at  $t = 0.94$  and  $0.96$ . The tidal field of the cluster has stripped material from the galaxy group, substantially increasing the luminosity at low surface brightness. This can be most easily seen as the low surface brightness plume emerging from the small group and extending to the upper right at

$t = 0.96$  (and even more extended at  $t = 1$  in the last panel of Figure 5).

This type of group accretion/interaction event is responsible for nearly all of the major ICL luminosity increases observed in our clusters. Typical events are characterized by group scale interactions stripping material from individual galaxies and beginning the production of diffuse light, followed by an accretion of the group into the denser cluster core which then generates significantly more ICL luminosity. Colloquially, the strong, close interactions in the group environment “soften up” the galaxies so that the large scale tidal field of the evolving cluster can more easily strip material from galaxies and form the ICL (see also Mihos 2004). The increases in the  $f_{ICL}$  function show that ICL luminosity in a cluster which formed by the accretion of groups is greater than the sum of the ICL luminosities of the individual groups alone.

### 3.3. Evolution of Very Faint ICL ( $\mu_V > 30.0$ )

One of the systematic effects imposed by our definition of ICL is that the ICL luminosity is dominated by the bright end of the defined magnitude range (see Figure 2). Thus, the above results are not truly sampling the entire range of ICL surface brightness. In order to trace the evolution of more faint ICL features, we have created another surface brightness cutoff at  $\mu_V = 30.0$  mag/arcsec<sup>2</sup>, and we define luminosity with equal or greater magnitude to be Faint ICL (FICL). Note that FICL luminosity is a subset of ICL luminosity, albeit only at a small fractional level.

The top of Figure 9 shows both the  $\Delta f_{ICL}$  and  $\Delta f_{FICL}$  functions, both calculated as described in Equation 1. The  $\Delta f_{FICL}$  function shows a very similar behavior to the  $\Delta f_{ICL}$  function, with changes in the  $f_{FICL}$  coming in short stochastic events. However, while the two functions share many common characteristics, the evolution of the ICL and FICL are certainly not coincidental. Using the procedure described below, we find that certain segments of the  $\Delta f_{FICL}$  function are highly correlated with segments of the  $\Delta f_{ICL}$  function, provided that the  $\Delta f_{FICL}$  segments are shifted backward in time; i.e., the evolution of the FICL lags behind the evolution of the brighter ICL. This behavior can be seen in the second row of Figure 9, which overplots the shifted segments of the  $\Delta f_{FICL}$  function with the  $\Delta f_{ICL}$ .

In order to calculate the correlation between the two functions, we first map the functions onto a regular time grid by fitting them using a third order polynomial interpolation (Press et al. 1986), evaluated at regular intervals of  $dt = 0.001$ . Note that the lines in Figure 9 follow the interpolated functions whereas those in Figure 3 simply linearly connect the data points. The  $\Delta f_{ICL}$  function was then divided into running bins of  $\delta t = 0.1$ . For each bin, we shifted the entire  $\Delta f_{FICL}$  function backward in time by  $\Delta t = 0.0 - 0.1$  in steps of 0.001. For every value of  $\Delta t$ , we calculated the correlation coefficient,  $r$ , between the  $\Delta f_{ICL}$  function and the shifted  $\Delta f_{FICL}$  function, for those points in the bin of  $\delta t$ . The bottom plot of Figure 9 shows the maximum value of  $r$  calculated in each running bin ( $r_{max}$ ). The third plot down in Figure 9 shows the  $\Delta t$  shift associated with each of the  $r_{max}$  values ( $\Delta t_{max}$ ) which is greater than a threshold value of  $r_{thresh} = 0.85$ . The value of  $r_{thresh}$  was chosen subjectively to be the value of  $r_{max}$  above which the shape of the shifted  $\Delta f_{FICL}$  curve reasonably matched that of the  $\Delta f_{ICL}$  curve.

The colored curves in the second plot of Figure 9 correspond to the segments of length  $\delta t$  of the shifted  $\Delta f_{FICL}$  curve, shifted by the  $\Delta t_{max}$  of the highest value of  $r_{max}$  within each

contiguous set of running bins for which  $r_{max} > r_{thresh}$ . The colored segments of the top plot are the unshifted segments of  $\Delta f_{FICL}$  which are shown below.

This analysis illustrates two particularly interesting features. First, there does seem to exist a real correlation between the evolution of the ICL at different surface brightnesses, with a time lag between features seen at high and low surface brightness. However, while this correlation holds for significant portions of the clusters’ evolution, it does not hold universally for their entire evolutionary history. This suggests that while a similar mechanism may be driving the evolution of both high and low surface brightness ICL, there is a complex relationship between the two. Second, the time lag between high and low surface brightness features increases as a function of the cluster’s evolutionary age. This is illustrated by the third plot down in Figure 9. With only one exception in C2,  $\Delta t_{max}$  increases as function of time for all contiguous sets of  $r_{max} > r_{thresh}$ .

We suspect that this behavior is due to the changing dynamical scales on which stripping and ICL production is occurring during the evolution of the cluster. At early times, the proto-cluster is basically a collection of smaller groups, which have small physical dimensions and high density, leading to short dynamical timescales. When material is stripped in these environments, it quickly disperses to lower surface brightness, resulting in only a small time lag between the evolution of high and low surface brightness material. As the cluster evolves and grows by accreting these groups, both the cluster dynamical timescale and the physical size of the ICL grow; propagating large amounts of luminosity from high surface brightness to low takes more time and the time lag between the  $\Delta f_{ICL}$  and  $\Delta f_{FICL}$  functions grow. The complexity of cluster-wide stripping also explains why the correlation between the ICL and FICL is not universal: it happens only at times where the stripping and production of ICL is concerted throughout the volume. For example, the correlation is strong in all simulations at the beginning, when the galaxies are collapsing in the group environment throughout the simulation, as well as in clusters C2 and C3 at later times ( $t \approx 0.7$ ) when there is a cluster-wide collisional event.

### 3.4. ICL Morphology

As the clusters evolve, not only does the quantity of ICL evolve, but also the morphology of the ICL features changes dramatically. As seen in Figures 5–7, the ICL luminosity at very early times is simply the outer halos of individual galaxies (see §3.1.1 for a discussion of the simulations at early times). However, by  $t = 0.5 - 0.6$  each of the clusters show individual sub-groups which have developed small ICL halos, with very prominent long, thin tidal features, such as tails, streamers, and filaments. These narrow features can be relatively high in surface brightness ( $\mu_V < 29$ ), and would be detectable in current broad-band imaging studies — for example, see the large scale filaments and plumes visible in Abell 1914 (Feldmeier et al. 2004). As the evolution of the clusters progress, the amount of filamentary substructure decreases as the groups coalesce and the thin tidal streams mix together to form a more diffuse common envelope at much lower surface brightness, and with little substructure. This behavior argues that the morphology of the ICL, along with its quantity, hold a wealth of information about the cluster’s dynamical history. We defer a more quantitative morphological analysis of the ICL to future papers.

### 3.5. Radial Distribution of ICL in Evolved Clusters

We finish the discussion of the ICL structure in our simulated clusters by focusing on the radial distribution of ICL luminosity at late times. As shown in Figure 3, at late times in their evolutionary history the fractional ICL luminosity of the clusters is  $\approx 10\text{--}15\%$ . However, this number is measured over the cluster as a whole, and can vary significantly as a function of cluster radius. This variation is shown in Figure 10, where the fractional luminosity is plotted as a function of projected radius. In each case, the innermost radial bin, at  $R < 1.5R_{1/2}$ ,<sup>2</sup> has a very low ICL fraction of  $\approx 5\%$ . This low ICL fraction is due to the fact that the cluster cores are dominated by luminous galaxies whose high surface brightness envelopes nearly fill the projected area — there is no room for much ICL in the core. Outside the core, the filling factor of the galaxies drops but the dense environment is still conducive to tidal stripping, and here we see a sharp increase in the ICL luminosity fraction (20–50%, depending on the cluster). Further out from the core, clusters C1 and C3 show a smooth monotonic decrease in the ICL fraction; in the outskirts of the clusters, galaxies have not been subjected to the dynamical stripping that contributes so strongly to the formation of ICL. Cluster C2 shows significantly more variance, however. This is largely due to how the radial bins sample the galaxy population, and the presence of bright galaxies in a few of the radial bins. As a result, the ICL fraction in cluster C2 varies significantly depending on exactly which radial bin is being considered — for example, three bright galaxies all fall in the third radial bin in cluster C2, suppressing the ICL fraction in that bin.

The radial profiles shown in Figure 10 illustrate two important points. First, on average the ICL fraction shows a radial gradient, declining in the outer portions of the cluster similar to the ICL gradients observed in simulations by Murante et al. (2004). In general, we find that ICL luminosity is centrally concentrated compared to galactic luminosity, in agreement with the results of both Murante et al. (2004) and Willman et al. (2004). Second, the ICL fraction can vary significantly both between and within clusters, depending on where and how it is measured. This is due in part to the relatively low mass of our clusters — stochastic effects due to radial binning and the distribution of galaxies will be lessened in more massive clusters. Nonetheless, this effect demonstrates that local measurements of the ICL fraction in clusters based on observations with small areal coverage may not be indicative of the ICL fraction of the cluster as a whole.

## 4. SUMMARY

In this paper, we have used  $N$ -body simulations to model the dynamical evolution of galaxy clusters to study the formation and evolution of low surface brightness intracluster light. Using an observational definition for ICL to be at a surface brightness of  $\mu_V > 26.5 \text{ mag/arcsec}^2$ , we quantify the distribution and luminosity of the ICL as a function of cluster age, and link the production of ICL to dynamical events in a cluster’s evolutionary history. We also highlight the importance of the group environment in beginning the ICL stripping process which is then amplified as groups accrete to form the cluster.

Our findings suggest that the observed properties of the ICL contain a wealth of information about the evolutionary history and dynamical state of the cluster. In particular, we find that

as the cluster evolves luminous material is transferred from high to low surface brightness, causing a shift in the cluster’s luminosity profile as a function of surface brightness. This leads directly to the increasing fraction of the cluster luminosity found in the ICL. Because ICL production is driven by group accretion events within the cluster, the cluster’s ICL luminosity is a sensitive indicator of the cluster’s accretion activity. We have also shown that very low surface brightness ICL features are correlated with higher surface brightness ICL features but lag behind in time, which raises the possibility of using ICL features of different surface brightness to probe the clusters’ evolution deeper into its dynamical history. Additionally, we see a clear evolutionary trend in the morphology of ICL features. The long, thin tidal features which are so prevalent early in the cluster’s evolution, are destroyed as the cluster accretes, leading to a more diffuse and amorphous envelope at later times.

In evolved clusters, we find that  $\approx 10\text{--}15\%$  of our clusters’ luminosity is at ICL surface brightness. These numbers roughly agree with, but are on the low end of the  $\approx 10\text{--}40\%$  of cluster luminosity identified as ICL by other authors using either modeling (Murante et al. 2004; Willman et al. 2004; Sommer-Larsen et al. 2005) or direct observations (Ciardullo et al. 2004). However, it is important to remember when interpreting these data that they are being compiled using several different definitions of what constitutes ICL. Our definition based on a surface brightness cutoff has the advantages that it is readily and directly observable, and requires no kinematic data or modeling of galaxy mass profiles. However, due to the very low luminosity of our surface brightness limit of  $26.5 \text{ mag/arcsec}^2$ , our definition of ICL is likely to be rather conservative compared to the definitions of others. Our results are in excellent agreement with the results of Feldmeier et al. (2004) who found isophotal ICL fractions between  $\approx 7\text{--}15\%$  in four Abell clusters when using a surface brightness limit of  $\mu_V = 26.5 \text{ mag/arcsec}^2$ . Also, it is worth noting the result of Murante et al. (2004) which finds that there is a positive correlation between cluster mass and ICL luminosity fraction. Our simulated clusters, being of relatively low mass, might then be expected to have a somewhat smaller fraction of their luminosity as ICL.

We find that the fraction of cluster luminosity contained in the ICL tends to increase with time, but does so in a very non-uniform manner. The production of ICL luminosity appears to be linked to group accretion events, and is thus a stochastic process intimately tied to the specific evolutionary history of the cluster. We note that Willman et al. (2004) claim to see only a weak correlation between accretion events and the fraction of unbound stars. While some of the discrepancy may be due to the differing definitions of ICL, another key difference is in the masses of the clusters studied. Willman et al. looked at Coma-sized clusters, an order of magnitude more massive than the clusters studied here. The deep potential well of such massive clusters will continually and passively strip luminosity from member galaxies to a greater extent than in these low mass clusters, possibly leading to markedly different ICL evolution in clusters of significantly different mass. However, there exists yet another major difference between the two analyses, which is the different scales on which we identify accretion events. Willman et al. follow only the large scale accretion of mass into the cluster potential. Our analysis, however, is focused on the accretion of and interactions between small groups of galaxies within the cluster (see a similar analysis by Gnedin 2003). We find that the production of

<sup>2</sup>  $R_{1/2}$  is the half-light radius of the cluster,  $\approx 150\text{--}200 \text{ kpc}$  for these clusters.

ICL is highly correlated with these small scale events between groups and sub-groups within the cluster, but not necessarily the mass accretion history of the cluster as a whole.

In summary, the correlations seen here between the properties of the ICL and the evolution of galaxy clusters means that measurements of the ICL provide a powerful new tool for studying the dynamical history of clusters. Continuing investigations into low surface brightness ICL features — including studies of their luminosity, morphology, and kinematics, as well as the physical linkage to individual galaxies —

should reveal unprecedented information about the evolution of galaxy clusters and groups, and the processes affecting the evolution of the galaxies within them.

CSR appreciates support from the Jason J. Nassau Graduate Fellowship Fund. JCM acknowledges research support from the NSF through grant ASTR 98-76143 and from a Research Corporation Cottrell Scholarship.

#### REFERENCES

- Adami, C., Slezak, E., Durret, F., Conselice, C. J., Cuillandre, J. C., Gallagher, J. S., Mazure, A., Pelló, R., Picat, J. P., & Ulmer, M. P. 2005, *A&A*, 429, 39
- Agueri, J. A. L., Gerhard, O. E., Arnaboldi, M., Napolitano, N. R., Castro-Rodríguez, N., & Freeman, K. C. 2005, *AJ*, 129, 2585
- Arnaboldi, M., Freeman, K. C., Mendez, R. H., Capaccioli, M., Ciardullo, R., Ford, H., Gerhard, O., Hui, X., Jacoby, G. H., Kudritzki, R. P., & Quinn, P. J. 1996, *ApJ*, 472, 145
- Arnaboldi, M., Gerhard, O., Aguerri, J. A. L., Freeman, K. C., Napolitano, N. R., Okamura, S., & Yasuda, N. 2004, *ApJ*, 614, L33
- Berlind, A. A., & Weinberg, D. H. 2002, *ApJ*, 575, 587
- Byrd, G., & Valtonen, M. 1990, *ApJ*, 350, 89
- Ciardullo, R., Mihos, J. C., Feldmeier, J. J., Durrell, P. R., & Sigurdsson, S. 2004, *IAU Symposium*, 217, 88
- Da Rocha, C., & de Oliveira, C. M. 2005, *MNRAS*, 364, 1069
- Dressler, A. 1980, *ApJ*, 236, 351
- Dubinski, J. 1998, *ApJ*, 502, 141
- Durrell, P., Ciardullo, R., Feldmeier, J. J., Jacoby, G. H., & Sigurdsson, S. 2002, *ApJ*, 570, 119
- Feldmeier, J. J., Ciardullo, R., & Jacoby, G. H. 1998, *ApJ*, 503, 109
- Feldmeier, J. J., Mihos, J. C., Morrison, H. L., Harding, P. H., Kaib, N., & Dubinski, J. 2004, *ApJ*, 609, 617
- Feldmeier, J. J., Mihos, J. C., Morrison, H. L., Rodney, S. A., & Harding, P. H. 2002, *ApJ*, 575, 779
- Gal-Yam, A., Maoz, D., Guhathakurta, P., & Filippenko, A. V. 2003, *AJ*, 125, 1087
- Gerhard, O., Arnaboldi, M., Freeman, K. C., Kashikawa, N., Okamura, S., & Yasuda, N. 2005, *ApJ*, 621, L93
- Gnedin, O. Y. 2003, *ApJ*, 582, 141
- Gonzalez, A. H., Zabludoff, A. I., Zaritsky, D., & Dalcanton, J. J. 2000, 536, 561
- Gudehus, D. H. 1989, *ApJ*, 340, 661
- Hernquist, L. 1990, *ApJ*, 356, 359
- Hernquist, L. 1993, *ApJS*, 86, 389
- Holmberg, E. 1958, *Medd. Lund, Ser. 2*, No 136
- Merritt, D. 1984, *ApJ*, 276, 26
- Mihos, J. C. 2004, *Clusters of Galaxies: Probes of Cosmological Structure and Galaxy Evolution*, 277
- Mihos, J. C., Harding, P. H., Feldmeier, J. J., & Morrison, H. L. 2005, *ApJ*, 631, L41
- Moore, B., Katz, N., Lake, G., Dressler, A., & Oemler, A. 1996, *Nature*, 379, 613
- Moore, B., Lake, G., & Katz, N. 1998, *ApJ*, 495, 139
- Murante, G., Arnaboldi, M., Gerhard, O., Borgani, S., Cheng L.M., Diaferio, A., Dolag, K., Moscardini, L., Tormen, G., Tornatore, L., & Tozzi, P. 2004, *ApJ*, 607, L83
- Napolitano, N. R., Pannella, M., Anranboldi, M., Gerhard, O., Aguerri, J. A. L., Freeman, K. C., Capaccioli, M., Ghinga, S., Governato, F., Quinn, T., & Stadel, J. 2003, *ApJ*, 594, 172
- Neill, J. D., Shara, M. M., & Oegerle, W. R. 2005, *ApJ* 618, 692
- Oemler, A. 1973, *ApJ*, 180, 11
- Press, W. H., Flannery, B. P., Teukolsky, S. A., & Vetterling, W. T. 1986, *Numerical Recipes* (Cambridge:Cambridge University Press)
- Sommer-Larsen, J., Romeo, D. A., & Portinari, L. 2005, *MNRAS*, 357, 478
- Springel, V., Yoshida, N., & White, S. D. M. 2001, *New Astronomy*, 6, 79
- Uson, J. M., Boughn, S. P., & Kuhn, J. R. 1991, *ApJ*, 369, 46
- Vílchez-Gómez, R., Pelló, R., & Sanhuja, B. 1994, *A&A*, 283, 37
- Willman, B., Governato, F., Wadsley, J., & Quinn, T. 2004, *MNRAS*, 355, 159
- Zibetti, S., White, S. D. M., Schneider, D. P., & Brinkmann, J. 2005, *MNRAS*, 358, 949
- Zwicky, F. 1951, *PASP*, 62, 61



TABLE 1  
PROPERTIES OF THE SIMULATED CLUSTERS

Cluster	$R_{200}$ (Mpc)	$M_{200}$ ( $M_{\odot}$ )	$N_{gal}$ ( $z = 2$ )	$N_{gal}$ ( $z = 0$ )
C1	0.95	$9.3 \times 10^{13}$	121	75
C2	0.94	$9.1 \times 10^{13}$	143	89
C3	0.98	$1.0 \times 10^{14}$	164	106

FIG. 1.— A simulated image of Cluster C2 at  $t = 0.67$ , color coded by  $V$ -band surface brightness,  $\mu_V$ . Black represents all luminosity at  $\mu_V < 26.0$  mag/arcsec<sup>2</sup>. Each other color represents a bin of one mag/arcsec<sup>2</sup>: red is  $\mu_V = 26.0 - 27.0$ , orange is  $\mu_V = 27.0 - 28.0$ , etc. This same color scheme will be used in all simulated images shown in this paper. The distance scale in the upper right indicates the length of one megaparsec in physical units.

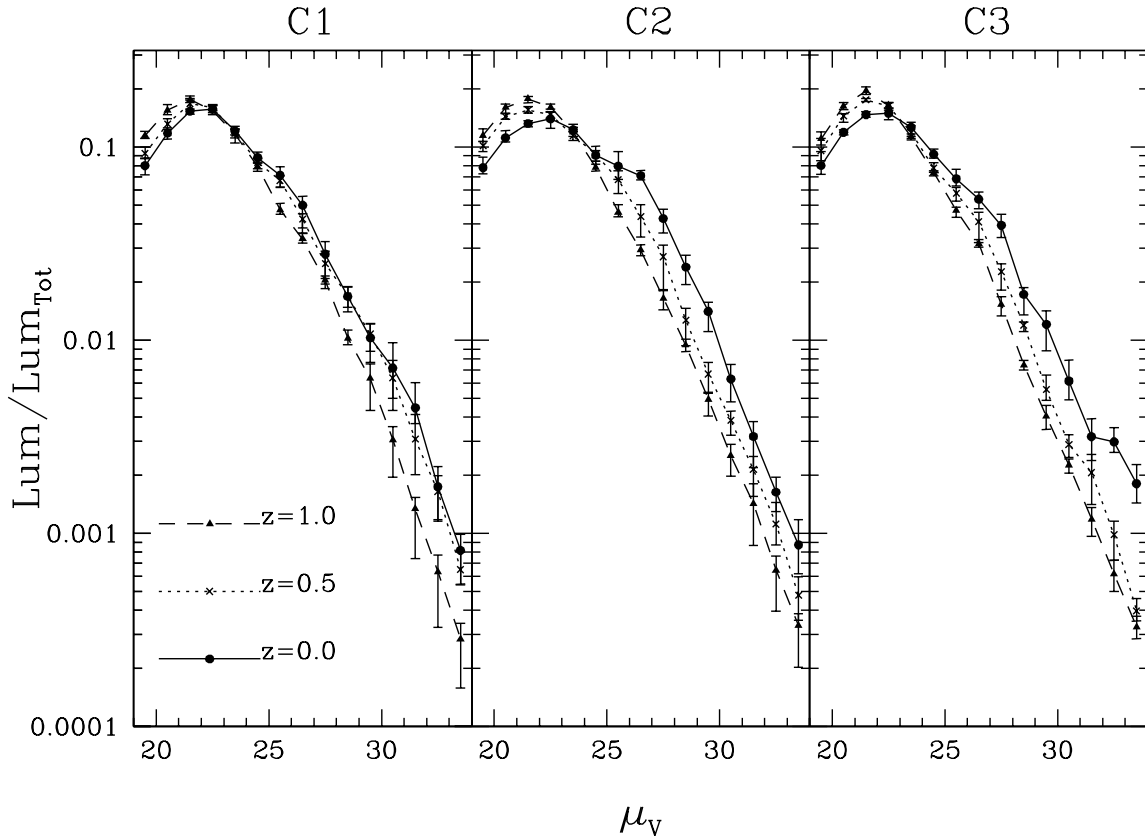


FIG. 2.— The fraction of cluster luminosity contained in 1 mag/arcsec<sup>2</sup> bins of  $\mu_V$  for each of the three clusters at three different timepoints in their evolution.

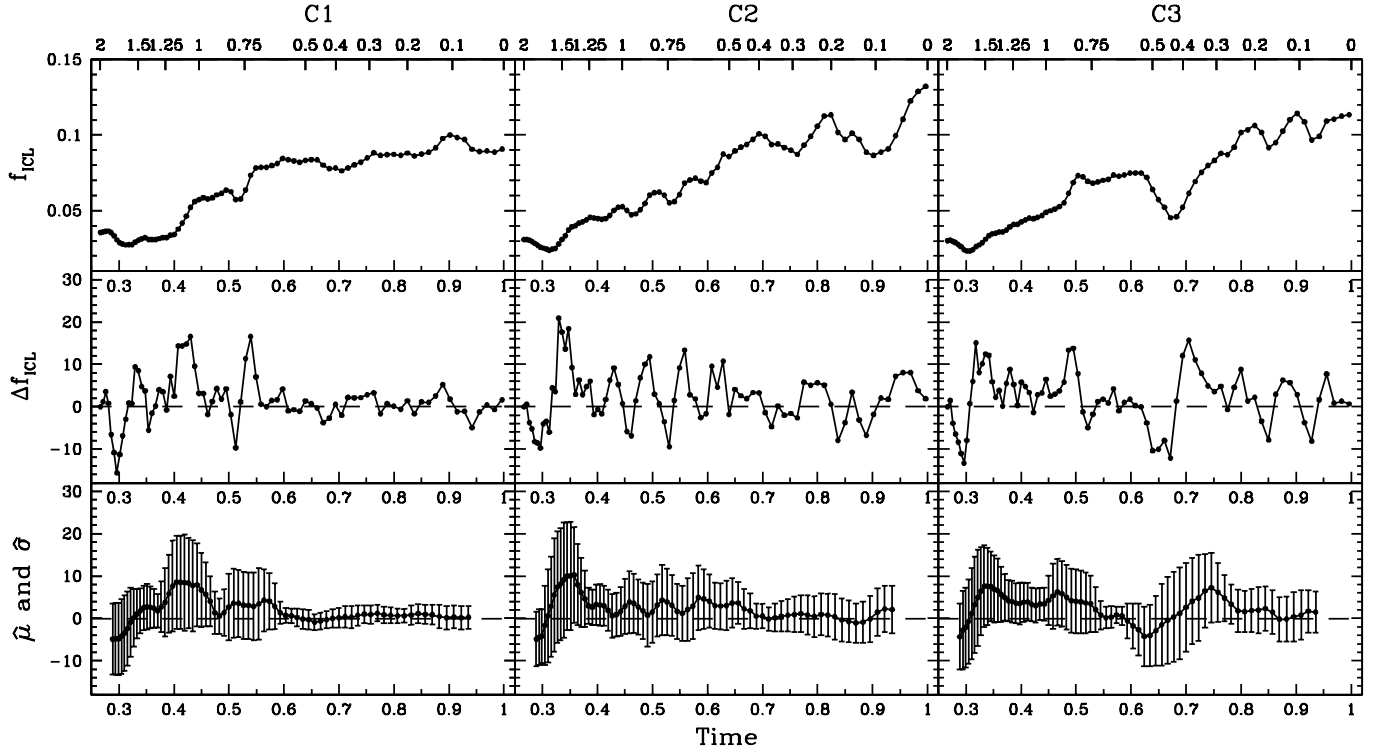


FIG. 3.— *Top*: The fraction of the luminosity in each cluster which is at ICL surface brightness ( $\mu_V > 26.5$  mag/arcsec<sup>2</sup>) as a function of time ( $f_{ICL}$ ). The top axis shows the corresponding nominal redshift. *Middle*: The fractional change in ICL luminosity per unit time as a function of time ( $\Delta f_{ICL}$ ). *Bottom*: The running mean ( $\hat{\mu}$ ) with standard deviation ( $\hat{\sigma}$ ) error bars, using a running bin of ten time points, for the  $\Delta f_{ICL}$  function. The time is the average of the timepoints in each bin.

FIG. 4.— Simulated images of the evolution of Cluster C1 color coded by  $V$ -band surface brightness,  $\mu_V$ . Black represents all luminosity at  $\mu_V < 26.0$  mag/arcsec<sup>2</sup>. Each other color represents a bin of one mag/arcsec<sup>2</sup>: red is  $\mu_V = 26.0$ – $27.0$ , orange is  $\mu_V = 27.0$ – $28.0$ , etc. The color scale is identical to that used in Figure 1. The distance scale in the upper left indicates the length of one megaparsec in physical units.

FIG. 5.— Simulated images of the evolution of Cluster C2 color coded by  $V$ -band surface brightness,  $\mu_V$ . Black represents all luminosity at  $\mu_V < 26.0$  mag/arcsec<sup>2</sup>. Each other color represents a bin of one mag/arcsec<sup>2</sup>: red is  $\mu_V = 26.0$ – $27.0$ , orange is  $\mu_V = 27.0$ – $28.0$ , etc. The color scale is identical to that used in Figure 1. The distance scale in the upper left indicates the length of one megaparsec in physical units.

FIG. 6.— Simulated images of the evolution of Cluster C3 color coded by  $V$ -band surface brightness,  $\mu_V$ . Black represents all luminosity at  $\mu_V < 26.0$  mag/arcsec<sup>2</sup>. Each other color represents a bin of one mag/arcsec<sup>2</sup>: red is  $\mu_V = 26.0$ – $27.0$ , orange is  $\mu_V = 27.0$ – $28.0$ , etc. The color scale is identical to that used in Figure 1. The distance scale in the upper left indicates the length of one megaparsec in physical units.

FIG. 7.— Simulated images of a short section of the evolution C2 at high time resolution color coded by  $V$ -band surface brightness,  $\mu_V$ . Black represents all luminosity at  $\mu_V < 26.0$  mag/arcsec<sup>2</sup>. Each other color represents a bin of one mag/arcsec<sup>2</sup>: red is  $\mu_V = 26.0$ – $27.0$ , orange is  $\mu_V = 27.0$ – $28.0$ , etc. The color scale is identical to that used in Figure 1. The distance scale in the upper left indicates the length of one megaparsec in physical units. The arrow points to the small galaxy group which moves through the cluster core (see Section 3.2.4 for details).

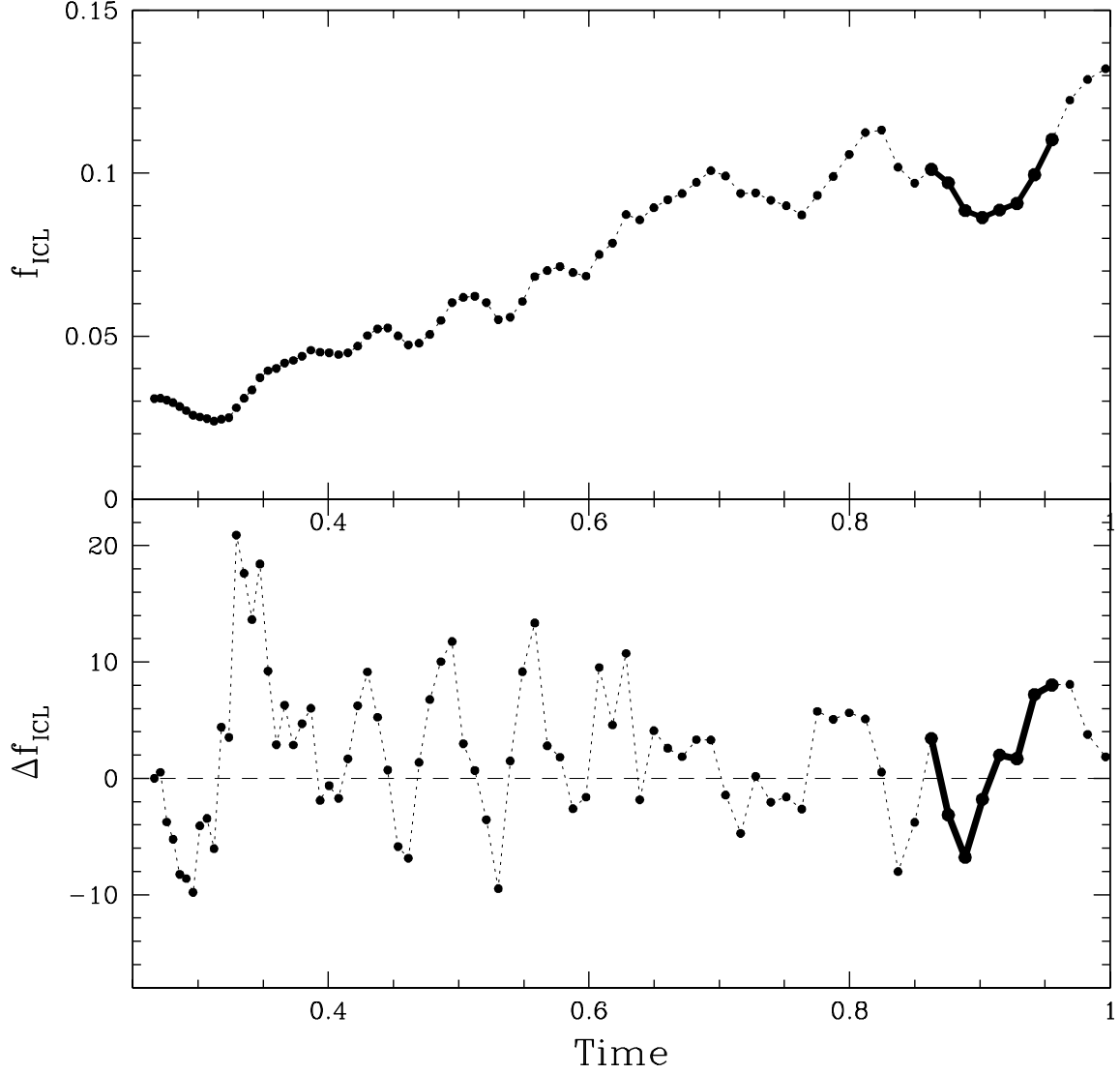


FIG. 8.— The  $f_{ICL}$  and  $\Delta f_{ICL}$  plots for C2. The bold section indicates the section used in the high time resolution analysis of §3.2.4.

FIG. 9.— *Top*: The  $\Delta f_{ICL}$  function for each cluster (closed circles) and the  $\Delta f_{FICL}$  function (open squares) which is simply the  $\Delta f_{ICL}$  function for luminosity at  $\mu_V > 30.0$ . The curves follow a third order polynomial fit to the data. The colored curves are those sections of the  $\Delta f_{FICL}$  which are highly correlated with sections of the  $\Delta f_{ICL}$ . *Middle Top*: The  $\Delta f_{ICL}$  function, with the highly correlated segments of the  $\Delta f_{FICL}$  function shifted in time by  $\Delta t_{max}$ . *Middle Bottom*:  $\Delta t_{max}$ , or the time shift which results in the highest correlation, for the highly correlated segments of the  $\Delta f_{FICL}$  function. *Bottom*: The highest value of the correlation coefficient,  $r$ , for each bin of the  $\Delta f_{FICL}$  function resulting from shifting  $\Delta f_{FICL}$  backward in time by  $\Delta t < 0.1$ .

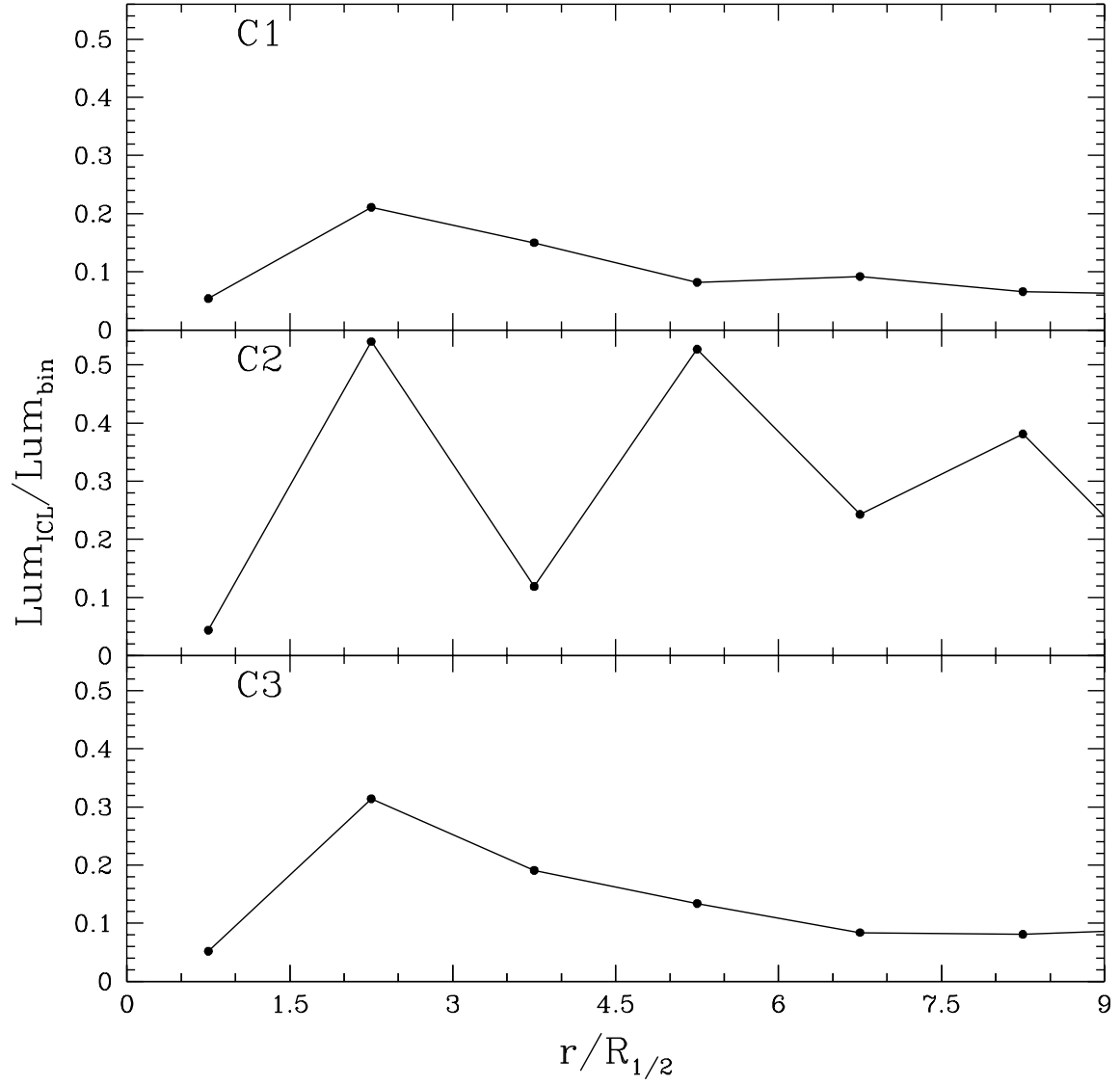
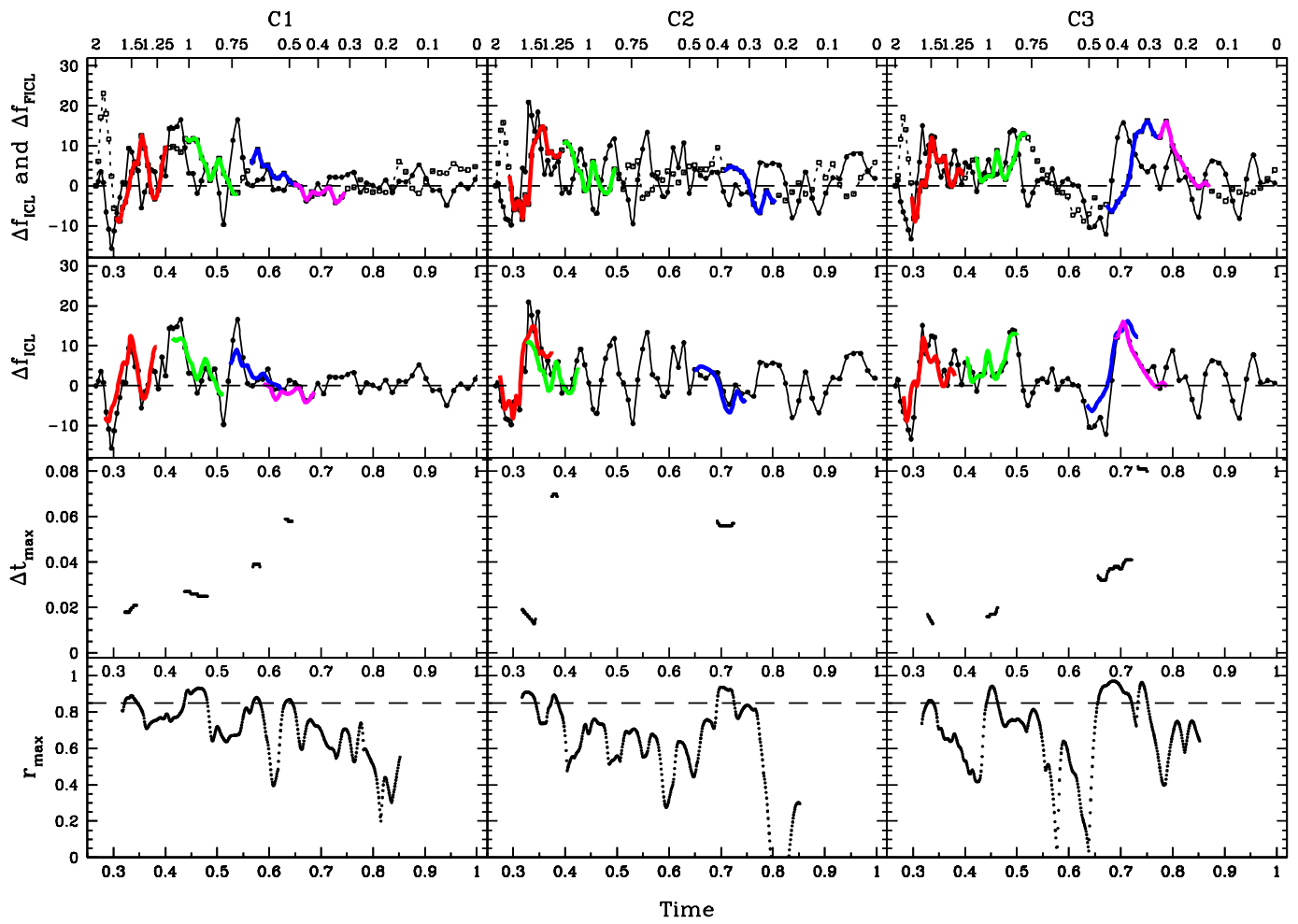


FIG. 10.— The fraction of ICL luminosity as a function of projected radius in each of the three simulated clusters.



This figure "figure1.png" is available in "png" format from:

<http://arxiv.org/ps/astro-ph/0605603v1>

This figure "figure4.png" is available in "png" format from:

<http://arxiv.org/ps/astro-ph/0605603v1>

This figure "figure5.png" is available in "png" format from:

<http://arxiv.org/ps/astro-ph/0605603v1>



This figure "figure6.png" is available in "png" format from:

<http://arxiv.org/ps/astro-ph/0605603v1>

This figure "figure7.png" is available in "png" format from:

<http://arxiv.org/ps/astro-ph/0605603v1>